# Journal of Environmental Sciences

**JOESE 5**


# Application of Remote Sensing and Ground Penetrating Radar for Evaluating the Groundwater Potentiality of West Qena Area, Egypt


**Ahmed Gaber[1], Adel Kamel Mohamed[2], Ahmed ElGalladi[2], Ahmed M. Beshr[2]**

*[1]Geology Department, Faculty of Science, Port-Said University*
*[2]Geology Department, Faculty of Science, Mansoura University*
E-mail: beshr@mans.edu.eg


***Reprint***


**Volume 48, Number 2: 74-86**
**(2019)**

**http://Joese.mans.edu.eg**

**P-ISSN 1110-192X**
**e-ISSN 2090-9233**

*Journal of Environmental Sciences, 2019; Vol. 48, No. 2: 55- 66*

**Journal of Environmental Sciences**
**JOESE 5**
**ISSN 2090-9233**

*Journal homepage http://Joese.mans.edu.eg*

*Original Article*

# Application of Remote Sensing and Ground Penetrating Radar for Evaluating the Groundwater Potentiality of West Qena Area, Egypt

**Ahmed Gaber[1], Adel Kamel Mohamed[2], Ahmed ElGalladi[2], Ahmed M. Beshr[2]**

[1]*Geology Department, Faculty of Science, Port-Said University*
[2]*Geology Department, Faculty of Science, Mansoura University*

E-mail: beshr@mans.edu.eg

**Article Info**

**Article history:**
Received
Received in revised form
Accepted

**Keywords:**
lineament,
fracture,
recharge,
infiltration,
InSAR,
coherence

## Abstract

Mapping the structural lineaments/fractures is of great importance for evaluating the groundwater potentiality, especially in hard rock terrains where they play as conduits and control the hydrogeological processes. This study demonstrates the efficiency of remote sensing imagery for mapping the lineaments in the Western Limestone Plateau and the low desert alluvial floodplain of the Nile west of Qena City. Different remote sensing data were used, including the SRTM DEM, Landsat-8, ALOS/PALSAR, and Sentinel-1 InSAR coherence images. They were processed to enhance the edge linear features by applying the hillshade algorithm on the DEM using ArcMap, the Sobel directional filter on the Landsat-8 image using ENVI, and the Pauli classification on the ALOS PALSAR image using SNAP. The lineaments were extracted from the processed images through on-screen digitizing in the ArcMap to produce the final lineament map. The lineaments have been confirmed from the Sentinel-1 InSAR coherence image. Moreover, GPR profiles have been acquired and carried out at discrete localities at the low desert alluvial floodplain. The extracted lineaments were statistically analyzed, and the results were displayed in the form of a rose diagram and a lineaments density map. The rose diagram has indicated that the area is affected by fractures of different lengths and structural trends; mostly NW-SE and some NE-SW. All of them occupy the plateau, while the low desert floodplain is free of lineaments. The plateau has a lineament density ranging from 0 to 1.21 km/km2. The high-density zones are of a high fracturing degree reflecting their high groundwater potentiality compared to the low-density zones. The study led to the classification of the area into zones of different groundwater potentiality ranging from very poor to very good. The potentiality of the plateau increases eastward as the lineament density increases.

## 1. Introduction

In arid environments, rainfall is scarce, irregular, unpredictable, and very low throughout the year. In such zones, the groundwater represents the main resource to meet the needs for water in the domestic, agricultural, and industrial purposes. The groundwater aquifers occur either in unconsolidated granular sediments, such as sands and gravels or in fractured calcareous and igneous rocks. In the unconsolidated clastic sediments, the groundwater occupies the pores and voids between the rock grains (primary porosity). However, the hard rocks have very poor or no primary porosity; the occurrence of groundwater depends on the rock secondary porosity that occurs along fractures, faults, fissures, and cracks (MacDonald et al., 2005). Evaluation of the groundwater potentiality of a hard rock terrain requires mapping the fracture zones and determining the degree of fracturing.

Remote sensing imagery is considered an effective tool for mapping the fractures, especially in the calcareous terrain to assess its groundwater potentiality (Waters et al., 1990; Sander et al., 1997; Meijerink et al., 2007; Sander, 2007). The term lineament is usually used to describe all of the mapped structural, topographical, vegetational, soil, and

* **Corresponding author**:
**Telephone**:
**E-mail:** *mahmoudi@mans.edu.eg*
*khaledgemail@yahoo.com*

lithological linear alignments, which are very likely to be the surface expression of buried structures, such as faults, fractures, joints, fissures, cracks, and shear zones that control the occurrence of groundwater (Singhal and Gupta, 2010). Berger (1984) suggested that for the lineaments to be linked to buried structures, they should satisfy one or more of the following criteria: (1) lineaments are aligned parallel to known structural trends; (2) lineaments are spatially coincident with subsurface structures interpreted from other datasets, such as gravity and magnetic data as well as radar satellites; and (3) lineaments represent surface features commonly associated with major subsurface structures, such as truncated features, sets of parallel faults, or structurally-controlled drainage patterns. Identifying the lineaments is of great importance in groundwater exploration, as they can act as conduits along which water infiltrates downward to recharge the subsurface aquifers; if they are interconnected, they can provide horizontal passageways for lateral groundwater movement; and if they are large enough, they might act as the groundwater storage zones themselves. Therefore, the zones where the lineaments intersect and occur with high density are areas of high groundwater potentiality for groundwater accumulation and can be suggested for performing further hydrogeophysical field survey and consequently drilling wells (Waters et al., 1990).

The aim of this study is to explore the groundwater potentiality of the Western Desert Limestone Plateau (calcareous terrain) and the low desert alluvial floodplain (unconsolidated sediments) west of Qena through lineament mapping that playing as conduits. This goal was achieved through analysis and interpretation of different optical and radar remote sensing data, including SRTM Digital Elevation Model (DEM), Landsat-8, ALOS PALSAR, Sentinel-1 InSAR coherence images. In addition, some geophysical GPR profiles collected at discrete localities were used to verify the results of the remote sensing data and to explore the near-surface structure and stratigraphy along the alluvial floodplain.

## 1. Study Area

The study area is a part of the Western Desert and located west of the cultivated floodplain of the Nile Valley at Qena Governorate between latitudes 25°47'N and 26°9'N and longitudes 31°51'E and 32°44'E (**Figure 1**). It comprises two parts: the low desert alluvial floodplain west the Nile Valley and the elevated Western Desert Calcareous Plateau. It is characterized by an arid desert climate; a hot summer from May to October and a mild winter from November to April. The maximum temperature reaches an average about 40.2 °C in summer and 28.4 °C in winter. The rainfall is scarce and occurs as scattered showers during winter. The total annual rainfall reaches about 3.2 mm/year (El-Khawaga, 2013; Radwan, 2018). There are no surface water resources running along the study area and the groundwater represents the only and main freshwater resource.

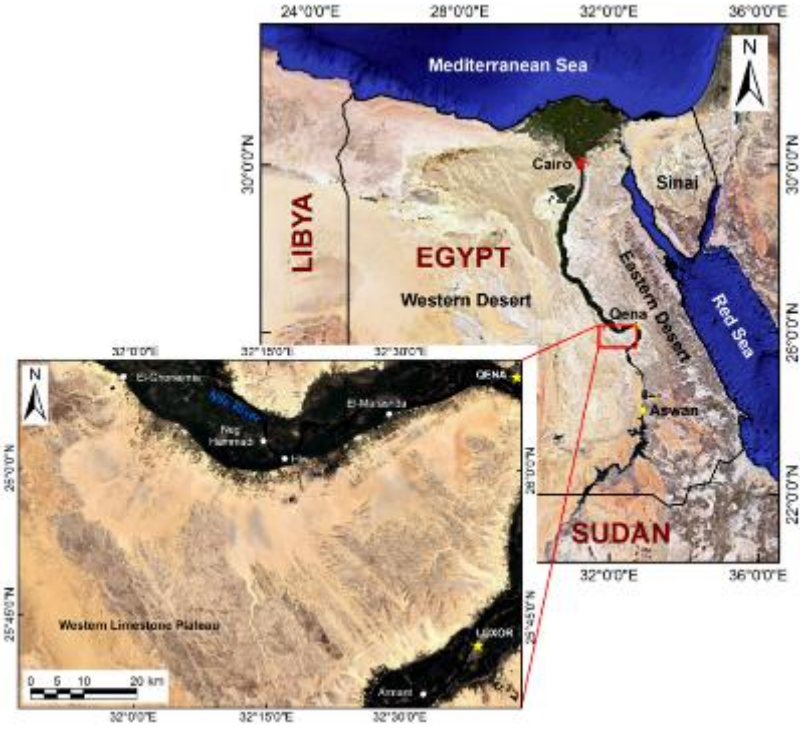


***Figure 1:*** *Location map of the study area.*

## 2. Geological and Tectonic Setting

The surface geological map of the study area, which was prepared from shows that the surface of the floodplain is covered by different alluvial sediments ranging in age from Pliocene to Quaternary, which include gravel, breccia, sand, silt, clay, and travertine deposits (**Figure 2**), (CONOCO and EGPC, 1987). These sediments were studied in detail by Said (1981) and Omer (1996), who divided them into a number of rock-units, which are from older to younger as the following:

- **Muneiha Formation (Pliocene):** marine clays intercalated with thin beds and lenses of silt and fine sand, overlain by fluvial sand, silt, and mud.
- **Issawia Formation (Pleistocene):** unbedded vesicular travertine topped by red talus breccia of angular limestone pebbles.
- **Qena Formation (Pleistocene):** cross-bedded sand with minor conglomerate and clay beds.
- **Fanglomerate (Pleistocene):** consolidated alluvial fan gravel sheets and other fine-grained clastic sediments.
- **Wadi deposits (Holocene-Recent):** loose silt, sand, and gravel.

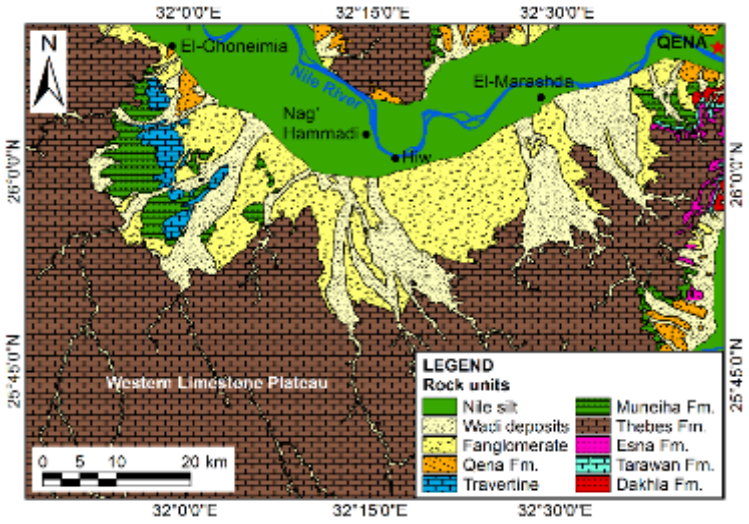


***Figure 2:*** *Geological map of the study area (CONOCO and EGPC, 1987).*

The western plateau represents the oldest exposed rocks in the area and is made up of a sedimentary succession ranging in age from Late Cretaceous to Early Eocene. It was dealt with by many authors, such as Faris et al. (1985); Faris et al. (1986); Abd El-Hameed (1994); Boukhary et al. (2011). They divided it into four rock-units, which are from older to younger: Dakhla Formation (Late Cretaceous-Paleocene, mainly shale), Tarawan Formation (Late Paleocene, mainly chalk), Esna Formation (Late Paleocene-Early Eocene, mainly shale), and Thebes Formation (Early Eocene, massive limestone).

Since the study area is a part of the so-called Qena Bend, it shares most of its tectonic setting. According to Youssef (2003); Akawy and Kamal El Din (2006); Abdelkareem and El-Baz (2015), the path of the Nile Valley is determined by structural features formed in response to the tectonic activities that took place in the Red Sea region during the Oligo-Miocene Age. At Qena region, the valley north of Nag' Hammadi is trending NW-SE parallel to the Gulf of Suez-Red Sea tectonic rift and/or uplift and east of Nag' Hammadi is trending NE-SW parallel to the Gulf of Aqaba and intersects from the east with the so-called Qena-Safaga shear zone.

## 3. Hydrogeological Setting

According to the geological setting, the groundwater-bearing units are either clastic or non-clastic carbonate rocks, which can be divided into two main aquifers namely; the Quaternary aquifer and the Eocene fractured carbonate aquifer (Hefny et al. (1992); Awad et al. (1997); RIGW (1997, 1998); El Tahlawi et al. (2008)). The Quaternary aquifer is the main groundwater bearing-unit at the cultivated lands and the desert fringes of the Nile Valley. It is composed mainly of the Pleistocene graded sand and gravel intercalated by clay lenses (i.e., Qena Formation), in addition to the Late Pliocene sands (i.e., upper part of Muneiha Fm.). It overlies the impermeable Pliocene clays (i.e., lower part of Muneiha Fm) that act as an aquitard preventing the connection between this aquifer and the deeper ones. Its water occurs under semi-confined conditions at the cultivated lands, as it is capped by the semi-impermeable Holocene agricultural silty-clay layer,

while occurs under unconfined conditions at the desert fringes due to its permeable cover of the wadi deposits. The Quaternary aquifer is recharged continuously from the excess irrigation water at the cultivated lands and the newly reclaimed lands, occasionally from rainfall, and probably from the upward leakage from the deeper aquifer through faults. It is discharged either through the transversal flow to the Nile or vertically through pumping to cover the agricultural and domestic needs.

The Eocene carbonate aquifer is unexplored and consists of the Early Eocene limestone of the Thebes Formation. This aquifer occurs within the Western Limestone Plateau and in the subsurface surrounding the Nile Valley. It is recharged possibly from the upward leakage from the deeper Nubian Sandstone aquifer through faults and occasionally from rainfall on the plateau.

## 4. Data and Methods

### *4.1. Optical and Radar Satellite Data*

In this study, the lineaments were delineated through the visual interpretation of different remote sensing images obtained by different optical and radar satellite sensors, including the SRTM DEM, Landsat-8, ALOS/PALSAR, and Sentinal-1 SAR images. The process of lineament extraction begins with some image processing or filtering to enhance or highlight the linear features of interest to facilitate identifying and tracing them. **Figure 3** shows the DEM of the study area, which was obtained from USGS (2019) with a 30 m spatial resolution. The lineaments were clarified from the DEM by applying the hillshade algorithm embedded in the ArcMap software of ESRI (2016) with light source azimuth angles of 45°, 90°, 135°, 180°, 225°, 270°, 315° (**Figure 3**).

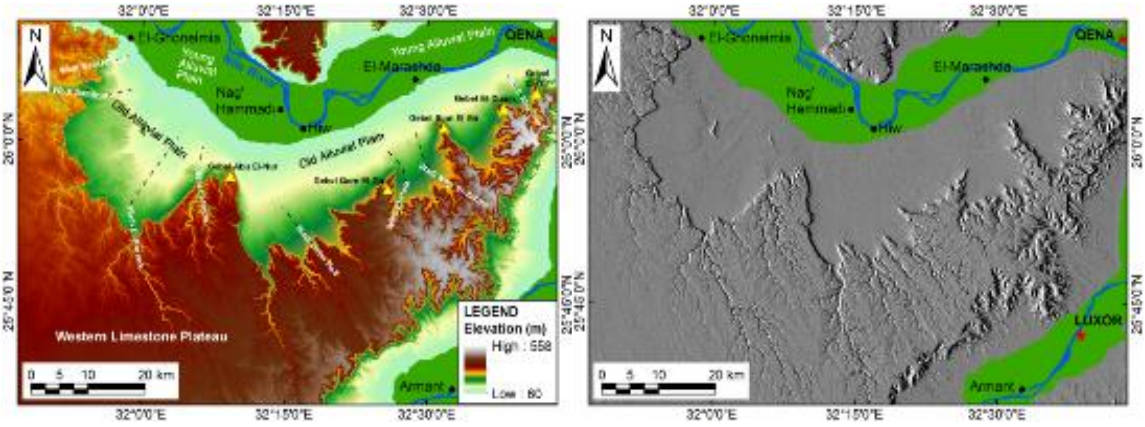


***Figure 3 :*** *STRM DEM of the study area (left) and the generated shaded relief map with light source azimuth angle of 45° (right).*

**Figure 4** shows the true-color composite image of the study area that was captured by the Landsat-8 Operational Land Imager (OLI) and produced by combining three spectral bands: band 4 as red, band 3 as green, and band 2 as blue (USGS, 2019). Landsat-8 OLI collects the image data in nine bands falling within the visible, near-infrared, and shortwave infrared spectrums with a spatial resolution of 30 m, except 15 m for the panchromatic band 8 (NASA, 2013). For this reason, the panchromatic band is usually selected for lineament mapping due to its high spatial resolution, in which the effect of moisture and contrast loss due to atmospheric haze is minimal (Suzen and Toprak, 1998). The so-called Sobel filter was applied to the panchromatic band to increase the contrast of the edge linear features to be much clearer (**Figure 4**) and brighter using the ENVI software of Exelis (2015). Sobel filter is a convolution filter, that uses a window size of 3×3 kernels of integer values in order to calculate the derivatives or gradients of the image intensity by convolving the window over the input image in the horizontal and vertical directions, respectively (Chang and Bai, 2018). Due to its directional nature, this filter is effective in enhancing the oriented linear features by convolving the window over the image in four principle directions (N-S, NE-SW, E-W, NW-SE), which their window kernels are listed in the **Table 1** (Suzen and Toprak, 1998).

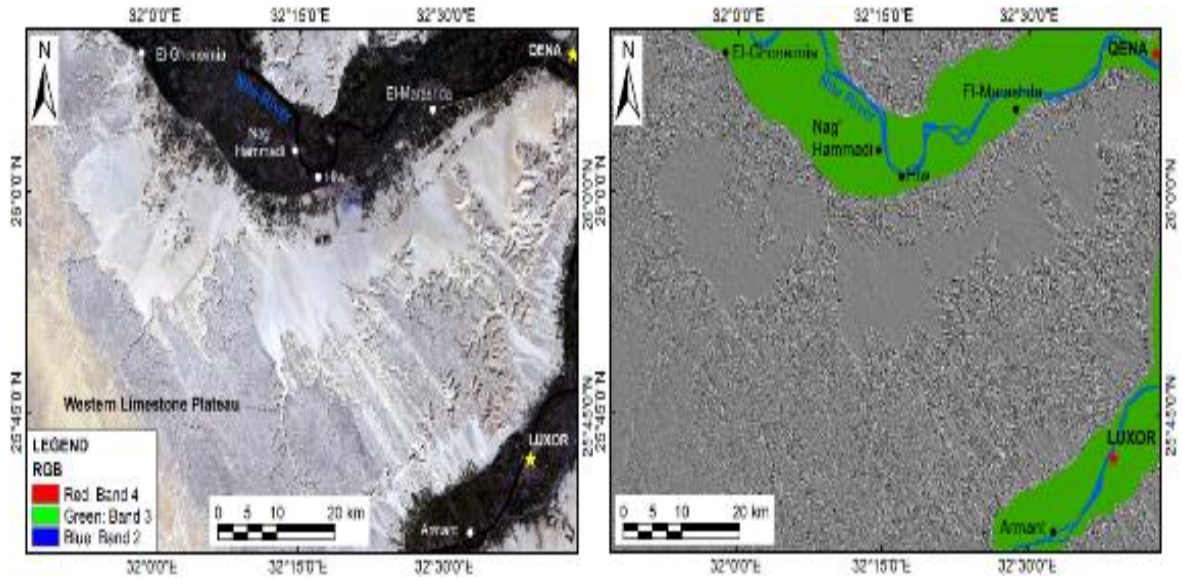


***Figure 4 :*** *True-color image of Landsat-8 for the study area (left) and the Sobel-filtered panchromatic band in the NW-SE direction (right).*

**Table 1** Sobel filter kernels in the four principle directions (Suzen and Toprak, 1998)

| N-S | | | NE-SW | | | E-W | | | NW-SE | | |
|---|---|---|---|---|---|---|---|---|---|---|---|
| -1 | 0 | 1 | -2 | -1 | 0 | -1 | -2 | -1 | 0 | 1 | 2 |
| -2 | 0 | 2 | -1 | 0 | 1 | 0 | 0 | 0 | -1 | 0 | 1 |
| -1 | 0 | 1 | 0 | 1 | 2 | 1 | 2 | 1 | -2 | -1 | 0 |

Therefore, the Synthetic Aperture Radar (SAR) satellite and its long wave radar images has been used in order to map any hidden or buried lineaments under the desert sand sheet that cover the study area. The satellite radar sensors are operating in longer electromagnetic wave signals than the optical and thermal sensors, thus it has the capability to penetrate the dry and loos sand cover and image any buried features (Gaber et al., 2018). In this work, the ALOS PALSAR L-band radar image (24 cm wavelength) was ordered and processed by applying the Pauli RGB classification using the SNAP software (ESA, 2017) to clarify any hidden linear features along the flat alluvium floodplain (**Figure 5**).

The linear features were then traced or digitized from the shaded relief maps, the Sobel directionally filtered images, and the ALOS/PALSAR radar image to produce the final lineament map of the study area (**Figure 6**). A Google Earth image was used to avoid or minimize tracing any of the non-geological or man-made linear features, which are not related to structures, such as roads, tracks, and field boundaries.

### *4.2. InSAR Coherence Change Detection*

The Interferometric Synthetic Aperture Radar (InSAR) coherence image represents the difference in the phase and intensity of the pixels of two SAR images acquired at different times. The InSAR coherence image enables the detection of very subtle small changes on the land surface of arid deserts, where the changes in the surface are usually due to the movement of mobile sand or the surface erosion due to aeolian and fluvial activities. This is because such dynamics cause changes in their respective radar intensity and backscattered response. It is used in this study to confirm the lineaments and to map the movement of windblown sand that might be controlled by structures. The method proved its efficiency for such purposes by Lee and Liu (2001); Liu et al. (2001); Catherine and André (2007); Bodart et al. (2009); Gaber et al. (2018); Gómez et al. (2018).

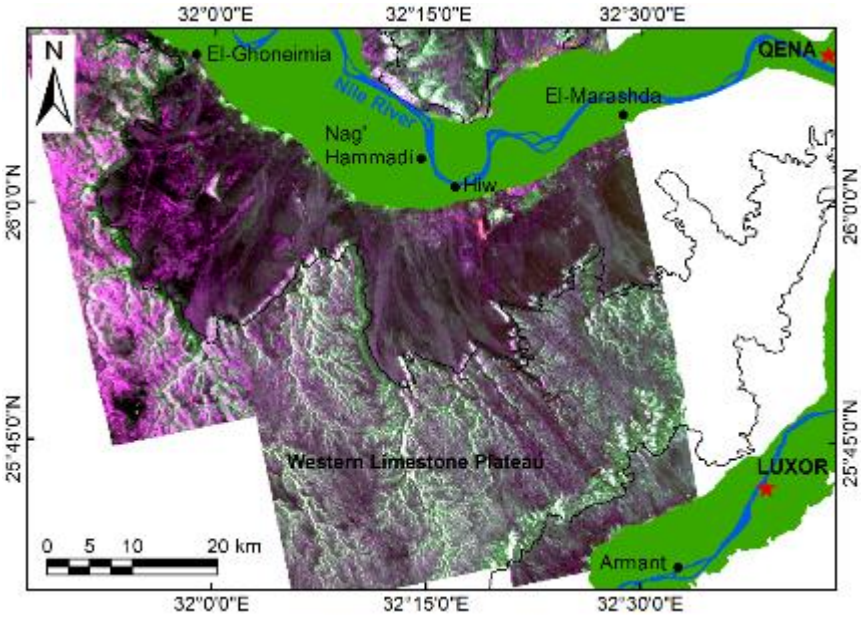


***Figure 5:*** *ALOS/ PALSAR Pauli RGB radar image of the study area.*

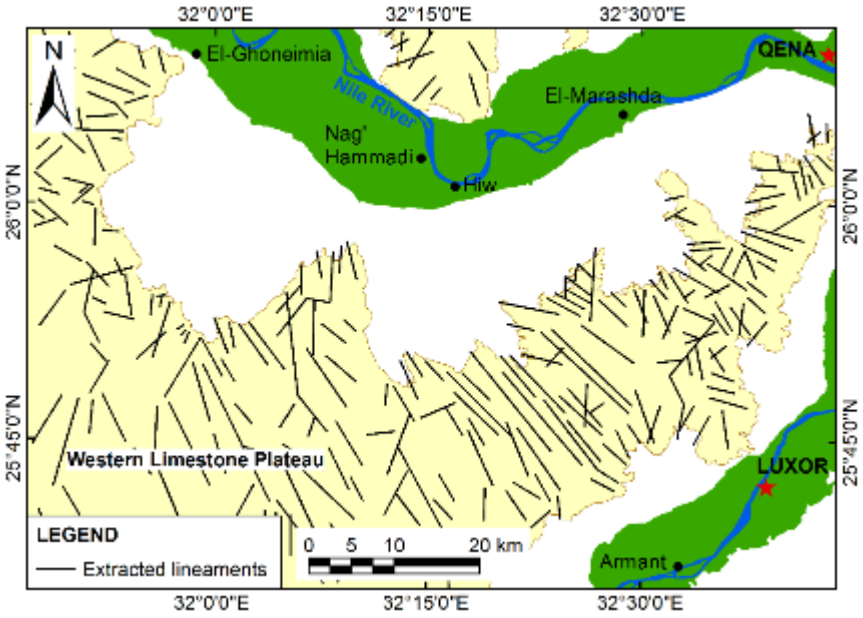


***Figure 6:*** *Final lineament map of the study area.*

The InSAR coherence image of the study area was derived from two Sentinel-1 C-band SAR images (5.6 cm wavelength) acquired at 7 August 2015 and 13 August 2016 with Vertical-Vertical (VV) polarization using SNAP software (**Figure 7**). It has an intensity ranging from 0 to 1. The high coherence (approaching 1) indicates a good match between the two image scenes acquired at different times, which reflects little or no changes in the land surface. On the other hand, the low coherence (approaching zero) is indicative of a prominent difference between the two image scenes, due to great changes in the land surface.

***4.3.***

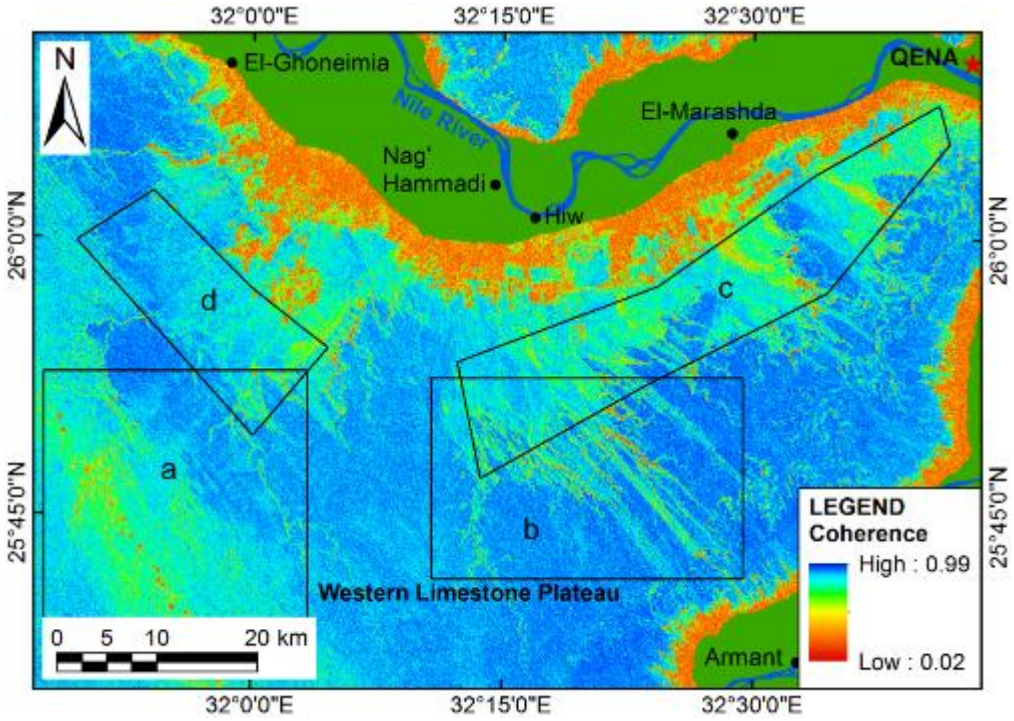


***Figure 7 :InSAR coherence image of the study area.***

### *4.4. Ground Penetrating Radar (GPR) Survey*

The Ground-Penetrating Radar (GPR) is a powerful tool for exploring the near-surface stratigraphy and the shallow geologic structures. It was used to verify the results of the optical and radar satellite images at the alluvial floodplain. A total of 13 GPR profiles were collected at discrete localities using the MALA ProEx GRR system, which utilizes shielded antenna with a frequency of 100 MHz. The transmitter sends repetitive short-duration electromagnetic (EM) signals into the ground as the antennas move across the surface. The EM waves propagate through the ground and reflected back to the receiver by the interfaces between the rocks of different properties. The geological conditions that can cause reflections include the lithological changes, layering, groundwater level, bedrock, boulders, cobbles, voids, faults, and cracks. The propagation of EM waves and their penetration depth depends on the conductivity and dielectric constant of the mediums. The GPR works best in the sandy and gravelly soils of low conductivity, while the clay soils attenuate the GPR signals strongly. The penetration depth and resolution depend on the Antenna frequency. The low frequencies achieve high penetration depths but with low resolutions as opposed to the high frequencies.

The Reflex software was used to display and process the collected GPR data by applying filters including Automatic Gain Control (AGC) and background removal (Sandmeier, 2014). The AGC filter serves for emphasizing of low amplitude ranges against ranges with high amplitudes, through multiplying each trace within the data by a scaling factor. The background removal filter is applied by subtracting the average of traces from the entire data to eliminate temporally consistent noise, suppress horizontally coherent energy, and emphasize signals, which vary laterally, such as diffractions and therefore make the true signals more visible. According to Jol (2009), an average dielectric constant of 4.5 was chosen for the dry sand and gravel that cover the surface of the study area for using in velocity estimation and time-to-depth conversion. **Figure 8** shows the processed GPR profiles. All of them penetrate about 7 m at 100 ns with a velocity of about 0.14 m/ns.

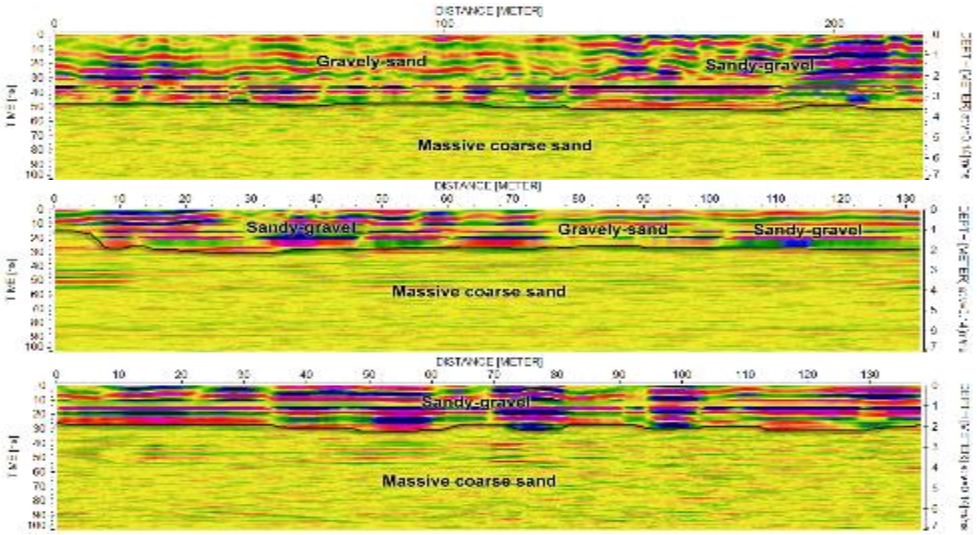


***Figure 8 :*** *Selective examples of the collected GPR profiles at the alluvial floodplain.*

## 5. Results and Discussion

The lineament map (**Figure 6**) shows that all of the extracted lineaments are confined to the outcropped Western Limestone Plateau, while the desert floodplain, which is covered by alluvium was very difficult to map any lineaments neither from the STRM DEM and Landsat-8 images nor from the ALOS/PALSAR and Sentinel-1 InSAR coherence images.

The lineaments were confirmed from the InSAR coherence image that was derived from the Sentinel-1 SAR images (**Figure 7**). At zone (a), the movement of sand dunes can be clearly observed as red patches of low coherence (approaching zero) aligned in the NW-SE structure direction, which cannot be detected neither on the Landsat-8 image nor the Google Earth image. The horns of dunes are directed in the SW, indicating that the wind blows and transports the sand in the SW direction. At zone (b), several green parallel wide linear features-oriented NW-SE having moderate coherence can be identified overlapping on lineaments. They indicate the activity of sand across these fractures, which are subjected to continuous variation in the volume of its sand fill due to aeolian activity, leading to change in the intensity of its respective radar response that can be observed clearly on the InSAR coherence image. Within the western part of the desert floodplain (zone c), large green patches of moderate coherence are observed near the plateau cliffs, which indicate the high changes on its surface due to windblown sand movement and surface erosion due to ephemeral fluvial activities. While, at the eastern part (zone d), the coherence is high (approaching 1), which is indicative that this part is less affected by windblown sand and fluvial erosion during the time difference between the two images. Therefore, the land reclamation at the eastern part is highly exposed to desertification due to mobile sand encroachment on the vegetation cover and soil erosion than the western part. The intensive afforestation for wind breaks around the newly reclaimed areas can serve in minimizing the desertification and preserving the soil. Near the cultivated floodplain, the coherence is very low (approaching zero) due to the rapid changes in the vegetation cover and soil moisture at the reclaimed lands.

The mapped lineaments were statistically analyzed according to their length and bearing azimuth and the results were displayed in the form of rose diagram and lineament density map. The rose diagram shows that the lineaments are of two trends, NW-SE and NE-SW (**Figure 9**). The NW-SE trending lineaments are the most prevalent and the longest. This trend is parallel to the Oligo-Miocene Gulf of Suez-Red Sea tectonically uplifted hills that were responsible for the creation of the Nile Valley cracks that resulted in detachment of the plateau into an eastern and western plateau (Issawi and McCauley, 1992, 1993; Abdelkareem and El-Baz, 2015), reflecting their structural nature. The NE-SW lineaments are short and of less significance. This trend is parallel to the Gulf of Suez and Qena-Sagaga shear zone. The prevalent of the NW-SE lineaments can give an indication that if these fractures are deep enough and interconnected, they can refer to the possible groundwater flow direction from the Eocene Limestone Aquifer to the Quaternary Aquifer of the desert floodplain.

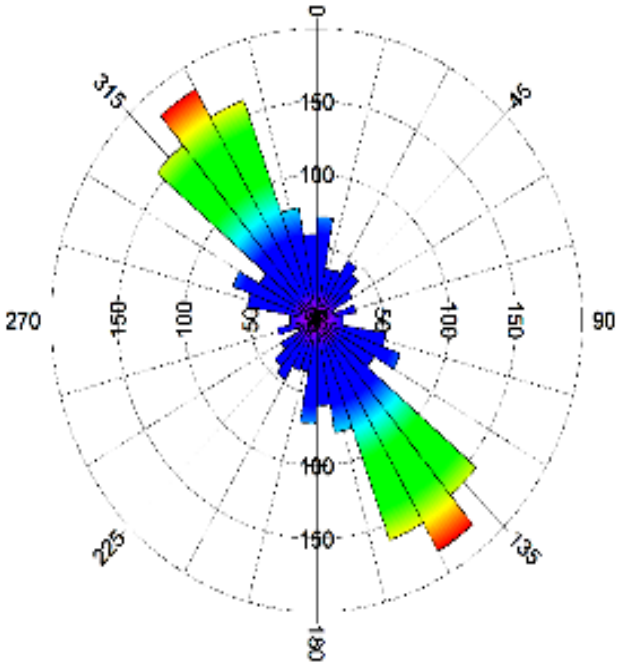


***Figure 9 :*** *Rose diagram of the extracted lineaments.*

The lineament density map is calculated from the total length of lineaments per unit area using ArcMap software (**Figure 10**). It is more related to the groundwater potentiality than individual lineaments. It shows that the area has a lineament density ranging from 0 to 1.21 km/km$^2$. The zones of high density are zones of high degree of fracturing, which is potential for water infiltration as opposed to the zones of low density. The highest lineament density can be observed on the eastern fringes of the plateau opposite Qena and decreases westward. This indicates that the groundwater potentiality is higher at the eastern part of the plateau than at its western part. This also indicates that the tensional force responsible for the creation of these cracks decreases westward as the distance from the Gulf of Suez-Red Sea uplift increases.

The lineament density map was classified with respect to groundwater potentiality on a descriptive scale (Very Good – Good – Fair – Poor – Very Poor) equivalent to a numerical scale ranging from 5 to 1, respectively (**Figure 11**). The areas of very high lineament density (0.96-1.21 km/km$^2$) are areas of very high infiltration and therefore were given the very good recharge rank, while the areas of very low lineament density (0-0.24 km/km$^2$) are areas of very low infiltration and hence were given very poor rank.

The GPR was used in this study to explore the near-surface structures at the desert floodplain due to the limitations of the optical and radar satellite images. The interpretation of the GPR profiles shows that the near-surface stratigraphy is similar across all profiles. It consists of two layers of different texture and composition separated by an erosional surface of aeolian and alluvial deposits, reflecting the deposition under different environments. The upper layer shows strong reflections and has a thickness varying from 2 to 4 m. The reflection amplitudes vary laterally within this layer reflecting its heterogeneous texture and composition and high porosity and permeability. It is interpreted as dry wadi deposits consisting of sheets of sandy gravel or gravely sand. The second layer shows lower homogeneous reflections, which was interpreted as dry massive coarse sand. Its lower boundary is not reached by GPR. This layer represents the uppermost part of the Qena Formation, which is considered the main water-bearing unit in the Nile Valley. The aquifer occurs under unconfined condition, due to its permeable wadi deposits cover. Similar to the satellite remote sensing data, no gross structures can be recognized from the GPR, reflecting the seismological stability of the desert floodplain. In the desert floodplain, the primary porosity plays the main role in the hydrogeological condition rather than rock fractures.

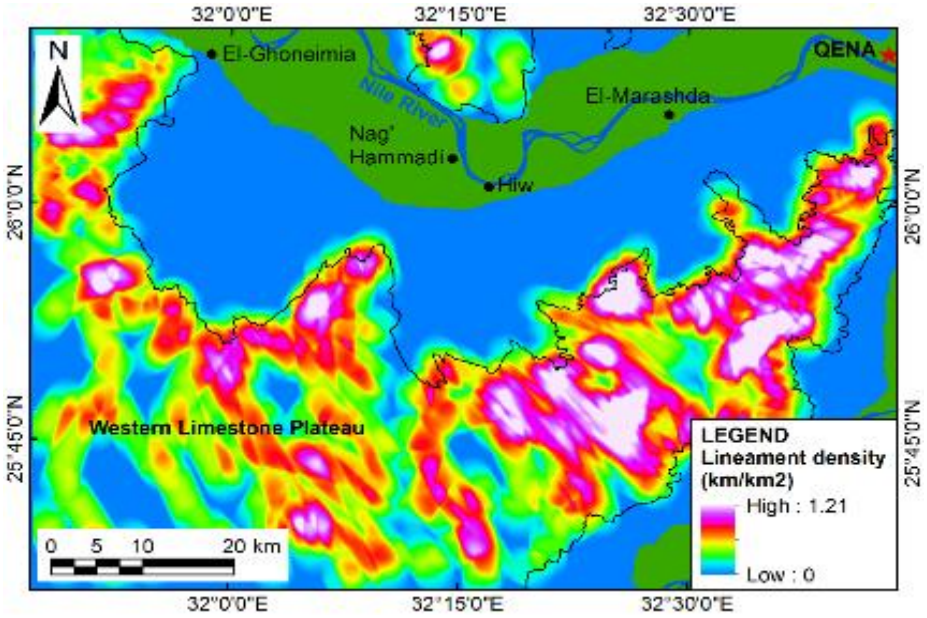


***Figure 10: Lineament density map of the study area.***

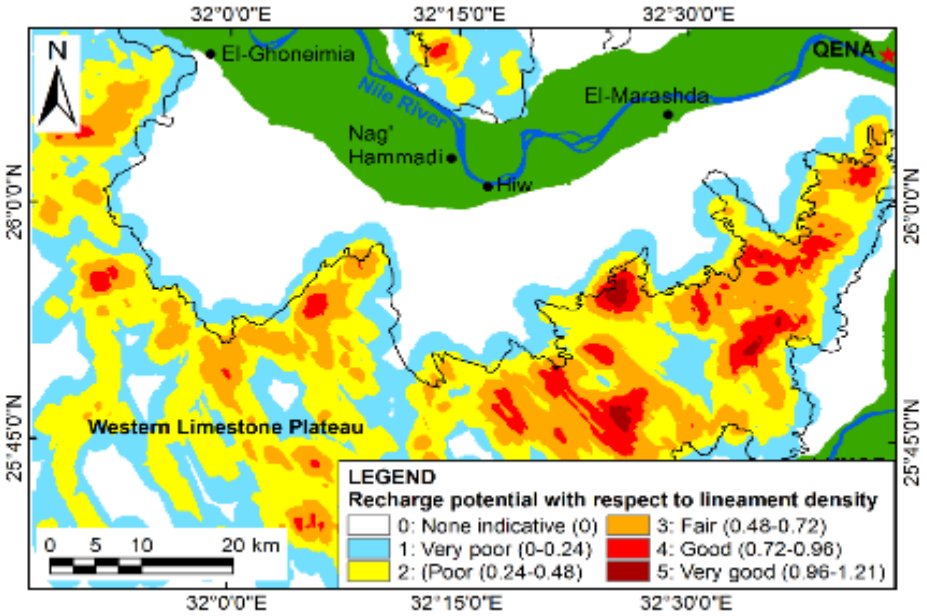


***Figure 11 Groundwater potentiality map with respect to lineament density of the study area.***

## 6. Conclusion

The study demonstrated the efficiency of remote sensing imagery in lineament mapping for assessing the groundwater potentiality of the Western Limestone Plateau and the alluvial floodplain of the area west of Qena Governorate. The lineaments were extracted from different optical and radar remote sensing data, including SRTM DEM, Landsat-8, ALOS PALSAR, and Sentinel-1 InSAR coherence images.

All of the extracted lineaments/fractures occupy the Western Limestone Plateau, while the floodplain was difficult to map any lineaments. They are of different lengths and related to structural trends; mostly trending NW-SE in the direction of the tectonically formed Gulf of Suez-Red Sea and some trending NE-SW parallel to the Gulf of Aqaba and Qena-Safaga shear zone, reflecting their structural nature. Therefore, the groundwater conditions on the plateau is controlled by the secondary porosity (fractures). The plateau has a

lineament density ranging from 0 to 1.21 km/km$^2$. The zones of high density are zones of high degree of fracturing, which is prerequisite for water infiltration and groundwater movement as opposed to the zones of low density. The lineament density on the plateau decreases westward as the distance from the Gulf of Suez-Red Sea increases, indicating that groundwater potentiality of the plateau decreases westward. The dominance of the NW-SE fractures is an indicative of the groundwater flow direction from the plateau towards the floodplain.

In addition, the GPR data proved that the floodplain has no shallow (near-surface) lineaments. The massive coarse sand of the Qena Formation that represents the main water-bearing aquifer is covered by 2-4 m thick wadi deposits layer, consisting of heterogeneous alluvial sediments of sandy gravel and gravely sand having high porosity and permeability. Therefore, the Quaternary aquifer occurs under unconfined condition.

## References


**Abd El-Hameed, A. T. (1994).** Petrographical characteristics and depositional environments of the Upper Paleocene-Lower Eocene sequence in Central Egypt. *Menoufia University Journal of Science, VIII*, 137-172.

**Abdelkareem, M., & El-Baz, F. (2015).** Mode of formation of the Nile Gorge in northern Egypt: a study by DEM-SRTM data and GIS analysis. *Geological Journal, 51*(5), 760-778. doi:10.1002/gj.2687

**Akawy, A., & Kamal El Din, G. (2006).** Middle Eocene to recent tectonics in the Qina area, Upper Egypt. *Neues Jahrbuch für Geologie und Paläontologie-Abhandlungen*, 19-51. doi:10.1127/njgpa/240/2006/19

**Awad, M. A., El Arabi, N. E., & Hamza, M. S. (1997).** Use of solute chemistry and isotopes to identify sources of ground-water recharge in the Nile aquifer system, Upper Egypt. *Groundwater, 35*(2), 223-228. doi:10.1111/j.1745-6584.1997.tb00078.x

**Berger, Z. (1984).** *Structural analysis of low-relief basins using Landsat data*. Paper presented at the International Symposium on Remote Sensing of Environment: 3rd Thematic Conference, Environmental Research Institute of Michigan, Ann Arbor.

**Bodart, C., Gassani, J., Salmon, M., & Ozer, A. (2009).** Contribution of SAR interferometry (from ERS1/2) in the study of aeolian transport processes: the cases of Niger, Mauritania and Morocco *Desertification and risk analysis using high and medium resolution satellite data* (pp. 129-136): Springer.

**Boukhary, M., Hussein-Kamel, Y., Abdelmalik, W., & Besada, M. (2011).** Ypresian Nummulites from the Nile Valley and the Western Desert of Egypt: their systematic and biostratigraphic significance. *Micropaleontology, 57*(1), 1-35.

**Catherine, B., & André, O. (2007).** *The use of SAR interferometric coherence images to study sandy desertification in southeast Niger: Preliminary results.* Paper presented at the Proc. Envisat Symposium', Montreux, Switzerland (ESA SP-636).

**Chang, N.-B., & Bai, K. (2018).** *Multisensor data fusion and machine learning for environmental remote sensing*: CRC Press.

**CONOCO, & EGPC (Cartographer). (1987).** Geological map of Egypt (Asyut and Luxor sheets). Scale 1:500,000.

**El-Khawaga, A. (2013).** Promoting irrigation water utilization efficiency in superior vineyards. *Asian Journal of Crop Science, 5*(2), 125-138. doi:10.3923/ajcs.2013.125.138

**El Tahlawi, M. R., Farrag, A. A., & Ahmed, S. S. (2008).** Groundwater of Egypt: "an environmental overview". *Environmental Geology, 55*(3), 639-652. doi:10.1007/s00254-007-1014-1

**ESA. (2017).** SNAP software (version 5.0): Sentinel Application Platform. Retrieved from http://step.esa.int/main/toolboxes/snap/

**ESRI. (2016).** ArcGIS Desktop 10.5 Help (includes ArcMap, ArcCatalog, ArcGlobe, and ArcScene softwares). Retrieved from https://www.arcgis.com/

**Exelis. (2015).** ENVI Classic 5.3 Help. Retrieved from https://www.harrisgeospatial.com/

**Faris, M., Abd El Monem, T., Abd El Hameed, & Marzouk, A. M. (1986).** The Cretaceous/Tertiary boundary in Taramsa section, west of Qena, Nile Valley, Egypt. *Newsletters on Stratigraphy, 16*(2), 85-97. doi:0078-0421186/0016-0085

**Faris, M., Allam, A., & Marzuk, A. M. (1985).** Biostratigraphy of the Late Cretaceous-Early Tertiary rocks in the Nile Valley (Qena region), Egypt. *Annals of the Geological Survey of Egypt, XV*, 287-300.

**Gaber, A., Abdelkareem, M., Abdelsadek, I., Koch, M., & El-Baz, F. (2018).** Using InSAR coherence for investigating the interplay of

fluvial and aeolian features in arid lands: implications for groundwater potential in Egypt. *Remote Sensing, 10*(6), 832. doi:10.3390/rs10060832

**Gómez, D., Salvador, P., Sanz, J., Casanova, C., & Casanova, J. (2018).** Detecting areas vulnerable to sand encroachment using remote sensing and GIS techniques in Nouakchott, Mauritania. *Remote Sensing, 10*(10), 1541. doi:10.3390/rs10101541

**Hefny, K., Farid, M. S., & Hussein, M. (1992).** Groundwater assessment in Egypt. *International Journal of Water Resources Development, 8*(2), 126-134. doi:10.1080/07900629208722543

**Issawi, B., & McCauley, J. (1992).** The Cenozoic rivers of Egypt: the Nile problem. In R. Friedman & B. Adams (Eds.), *The followers of Horus: Studies dedicated to Michael Allen Hoffman. Egyptian Studies Association Publication, no. 2, Oxbow Monograph 20* (pp. 121-146). Oxbow Books, Park End Place, Oxford, England.

**Issawi, B., & McCauley, J. (1993).** The Cenozoic landscape of Egypt and its river systems. *Annals of the Geological Survey of Egypt, 19*, 357-384.

**Lee, H., & Liu, J. G. (2001).** Analysis of topographic decorrelation in SAR interferometry using ratio coherence imagery. *IEEE Transactions on Geoscience and Remote Sensing, 39*(2), 223-232. doi:10.1109/36.905230

**Liu, J. G., Black, A., Lee, H., Hanaizumi, H., & Moore, J. M. (2001).** Land surface change detection in a desert area in Algeria using multi-temporal ERS SAR coherence images. *International journal of remote sensing, 22*(13), 2463-2477. doi:10.1080/01431160119991

**MacDonald, A., Davies, J., Calow, R., & Chilton, J. (2005).** *Developing groundwater: a guide for rural water supply*: ITDG publishing.

**Meijerink, A. M. J., Bannert, D., Batelaan, O., Lubczynski, M., & Pointet, T. (2007).** *Remote sensing applications to groundwater* (Vol. 16; IHP-VI Series on Groundwater): United Nations Educational Scientific and Cultural Organization (UNESCO).

**NASA. (2013).** Landsat Data Continuity Mission Brochure

**Omer, A. A. (1996).** *Geological, mineralogical and geochemical studies on the Neogene and Quaternary Nile Basin deposits, Qena-Assiut stretch, Egypt.* (Ph.D.), South Valley University, Sohag, Egypt.

**Radwan, M. (2018).** Geographic analysis of settlement sites of the desert back villages at Qena Governorate (in Arabic). *International Scientific Journal of Architecture, Engineering and Technology*, 13. doi:10.21625/baheth.v1i1.213

**RIGW (Cartographer). (1997).** Hydrogeological map of Egypt (Luxor sheet). Scale 1:500,000.

**RIGW (Cartographer). (1998).** Hydrogeological map of Egypt (Asyut sheet). Scale 1:500,000.

**Said, R. (1981).** *The geological evolution of the River Nile*: Springer-Verlag, New York, USA.

**Sander, P. (2007).** Lineaments in groundwater exploration: a review of applications and limitations. *Hydrogeology Journal, 15*(1), 71-74. doi:10.1007/s10040-006-0138-9

**Sander, P., Minor, T. B., & Chesley, M. M. (1997).** Ground‐water exploration based on lineament analysis and reproducibility tests. *Groundwater, 35*(5), 888-894. doi:10.1111/j.1745-6584.1997.tb00157.x

**Sandmeier, K. J. (2014).** REFLEXW software (version 7.2.3): A windows program for the processing and interpretation of reflection and transmission data.

**Singhal, B. B. S., & Gupta, R. P. (2010).** *Applied hydrogeology of fractured rocks* (2 ed.). Netherlands: Springer.

**Suzen, M., & Toprak, V. (1998).** Filtering of satellite images in geological lineament analyses: an application to a fault zone in Central Turkey. *International journal of remote sensing, 19*(6), 1101-1114. doi:10.1080/014311698215621

**USGS. (2019).** EarthExplorer website for downloading satellite remote sensing data. Retrieved from https://earthexplorer.usgs.gov/ (Last access 9 January 2019)

**Waters, P., Greenbaum, D., Smart, P. L., & Osmaston, H. (1990).** Applications of remote sensing to groundwater hydrology. *Remote Sensing Reviews, 4*(2), 223-264. doi:10.1080/02757259009532107

**Youssef, M. (2003).** Structural setting of central and south Egypt: an overview. *Micropaleontology, 49*(Supplement 1), 1-13. doi:10.2307/3648472